Blood Crystal: Emergent Order of Red Blood Cells Under Wall-Confined Shear Flow

Zaiyi Shen,[1,2] Thomas M. Fischer,[1,2,3] Alexander Farutin,[1,2]
Petia M. Vlahovska,[4] Jens Harting,[5,6] and Chaouqi Misbah[1,2,*]
[1]*Université Grenoble Alpes, LIPHY, F-38000 Grenoble, France*
[2]*CNRS, LIPHY, F-38000 Grenoble, France*
[3]*Laboratory for Red Cell Rheology, 52134 Herzogenrath, Germany*
[4]*Engineering Sciences and Applied Math, Northwestern University, Evanston 60208, USA*
[5]*Helmholtz Institute Erlangen-Nürnberg for Renewable Energy (IEK-11), Forschungszentrum Jülich, Fürther Strasse 248, 90429 Nürnberg, Germany*
[6]*Department of Applied Physics, Eindhoven University of Technology, P.O. Box 513, 5600 MB Eindhoven, Netherlands*

(Received 9 September 2017; revised manuscript received 12 April 2018; published 28 June 2018)

Driven or active suspensions can display fascinating collective behavior, where coherent motions or structures arise on a scale much larger than that of the constituent particles. Here, we report numerical simulations and an analytical model revealing that deformable particles and, in particular, red blood cells (RBCs) assemble into regular patterns in a confined shear flow. The pattern wavelength concurs well with our experimental observations. The order is of a pure hydrodynamic and inertialess origin, and it emerges from a subtle interplay between (i) hydrodynamic repulsion by the bounding walls that drives deformable cells towards the channel midplane and (ii) intercellular hydrodynamic interactions that can be attractive or repulsive depending on cell-cell separation. Various crystal-like structures arise depending on the RBC concentration and confinement. Hardened RBCs in experiments and rigid particles in simulations remain disordered under the same conditions where deformable RBCs form regular patterns, highlighting the intimate link between particle deformability and the emergence of order.

DOI: 10.1103/PhysRevLett.120.268102

Introduction.—Birds, fish, or even humans self-organize into captivating dynamic patterns on a scale much larger than the isolated unit [1–3]. In recent years, similar phenomena have been observed with active micro-units (either self-propelled or actuated by external fields) [4–8] such as bacteria [9,10], chemically-activated motile colloids and drops [11,12], vibrated grains [13–15], or electrically- and magnetically-driven colloids [16–18].

Flow fields constitute another way to drive the populations of microparticles (e.g., suspensions) into nonequilibrium ordered structures (e.g., microfluidic colloidal crystals [19–23]). Long-range hydrodynamic interactions between the fluid-embedded particles, i.e., correlations in the motions of particles mediated by flows in the suspending liquid, underly these self-organizing phenomena [24–26]. Another factor promoting order is confinement. If the bounding walls are removed, then the particles can pass over each other and experience hydrodynamical diffusion (a cross-flow displacement after collision) [27–30] that, like classical diffusion, favors homogenization (the intermixing of suspended entities) and tends to destroy any order. In microfluidic inertialess flows, drops [19,23,31–37] and red blood cells [38–40] have been observed to form a single file of regularly spaced cells.

Unlike for the microfluidic pressure-driven flows, structuring of microparticles under confined shear flows has been studied only to a limited extent, even though there are experiments showing the formation of trains in red blood cells (RBC) suspensions [41,42] and emulsions [43]. To fill this void, we carried out three-dimensional (3D) numerical simulations, motivated by experimental observations, to study the formation of two-dimensional (2D) arrays (crystals) by capsules and RBCs sheared between two parallel plates. We observe order, which intriguingly persists even when the size of the gap allows the particles to pass over each other; i.e., the emergence of order does not require strong confinement. We develop an analytical model that provides physical insight into the phenomena. The pattern wavelength (particle-particle separation) predicted by the model concurs well with simulations and experiments. It will be seen that the ordering is quite universal and should arise for a variety of systems.

The model.—The lattice Boltzmann method (LBM) [44,45] was used to solve the quasi-incompressible Navier-Stokes equations for fluid flow. The membrane energy consists of a contribution due to resistance to bending $(\kappa/2)H^2$, with H the mean curvature and κ the bending rigidity modulus, and resistance to in-plane shearing and stretching $\kappa_s(I_1^2 + 2I_1 - I_2)/12 + \kappa_\alpha I_2^2/12$, where κ_s is the shear elastic modulus, κ_α is the area dilation modulus, and I_1 and I_2 are the in-plane strain invariants (see [44]). $\kappa_\alpha/\kappa_s = 200$ is chosen large enough to preserve

local area conservation. The RBC size R is taken to be $R \simeq 4\ \mu$m. The reduced volume is defined as $\nu = (3V/4\pi)(A/4\pi)^{-3/2}$, with A the particle surface area and V its volume. $\nu = 0.64$ was used for the RBC model when compared with experiments, otherwise $\nu = 0.98$ was used (in this case, we refer to the cell as a capsule). This allowed computational efficiency without affecting order, provided that the particle is in the tank-treading (TT) regime. $C_{as} = \eta_0 \dot{\gamma} R/\kappa_s$ is the capillary number. C_{as} is set to 0.05. The viscosity contrast is fixed to one. The reference shape is taken to be the equilibrium one in the absence of shear elasticity. The suspension is sheared between two parallel planes at a constant shear rate $\dot{\gamma} = 2V/W$, where $2V$ is the relative velocity of the planes and W the channel width [Fig. 1(a)]. The Reynolds number $\mathrm{Re} = \rho \dot{\gamma} R^2/\eta_0$ (ρ is the density of the suspending fluid) is set to 0.5 in most of the simulations; it is sufficiently low so that inertial effects remain negligible [46–49].

The experimental set-up.—The experiments were performed in a homemade rheoscope with cone-plate geometry. Microscopic images were taken with a CCD camera (DMK 41BF02.H, The Imaging Source Europe GmbH, Bremen, Germany). Normal blood samples were obtained from the EFS (Etablissement Français du Sang) and kept refrigerated until use. Solid spherical particles were produced by suspending RBCs in an isotonic solution of sodium salicylate (Sigma-Aldrich), thus converting the biconcave RBCs into spheroechinocytes. This shape was then conserved by fixation with 0.25% glutaraldehyde (Alfa Aesar, Karlsruhe, Germany). RBCs and rigid spheres were washed three times with isotonic PBS (Dulbecco, biowest, Nuaille, France). RBCs or spheres were suspended in an isotonic solution of dextran (MW 500000D, Sigma-Aldrich, Saint-Quentin Fallavier, France) plus phosphate-buffered saline. The viscosity at room temperature (25 °C) was 50 mPa s (Anton Paar, Rheo plus, Graz, Austria), unless otherwise indicated. Suspensions of RBCs or spheres were prepared with volume fractions between 0.002 and 0.01 and were loaded into the cone-plate chamber. The shear rate was varied from 15 to 94 s^{-1}. The viscosity of the hemoglobin solution of healthy RBCs is around 10 mPa s at room temperature (25 °C). The experimental capillary number is in the range $C_{as} \simeq 0.75$–3. The aging of blood sometimes led to an echinocyte shape, which required significantly higher Ca.

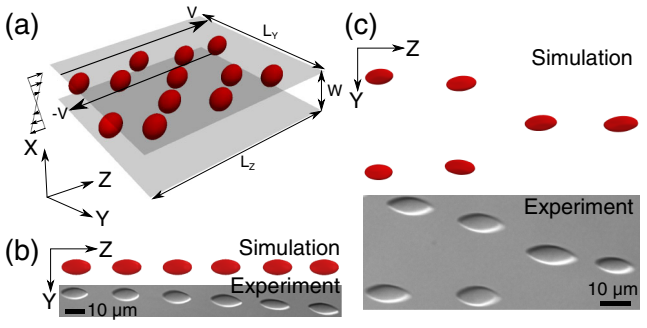

FIG. 1. (a) A schematic view of the simulation set-up. (b) Both the simulation and experiment show RBCs organized in stable chains along the flow direction; $W = 3R$ (R is the RBC radius defined in text.). The computational domain is $L_Y = 12R$, $L_Z = 30R$. (c) Chains can merge, resembling crystal dislocation.

Flow-aligned chains.—RBCs in a shear flow display two main types of dynamics, depending on the applied shear stress: TT at large shear stress, where the cell assumes a stable orientation relative to the applied shear direction, and tumbling at a low enough shear stress, where the cell executes a periodic flipping motion [50]. In both simulations and experiments, the parameters are chosen such that cells are in the TT regime. Experiments and simulations show the formation of regularly spaced chains of RBCs aligned with the flow direction, see Fig. 1(b) and Movie 1 and Movie 2 in [51].

Starting from a random initial cell distribution, we observe a transient regime during which cells mix (hydrodynamical diffusion), due to cell-cell hydrodynamic interactions, and migrate towards the midplane due to the hydrodynamic repulsion by the wall. Once all cells have reached the channel midplane, the degree of disorder decreases continuously until the cells reach an ultimate stable configuration of ordered chains [Fig. 1(b)]. Both experiments and simulations show that chains can merge into a stable Y configuration [Fig. 1(c)].

The finite ratio between the channel width W and cell size R is a crucial factor in the cell structuring. We find that a stable order is impossible if the cells were considered as points. An intriguing observation (analyzed in detail below) is that order persists even for weakly-confined suspensions (with the gap between planes about ten times the cell radius R), where one would have expected that cell-cell hydrodynamic interactions (responsible for hydrodynamic diffusion), pushing the cells out of the channel center, would allow the imposed shear flow to advect the cells further apart, thereby favoring disorder.

Crystals.—Numerical simulations show that at a low particle volume fraction, capsules form flow-aligned chains. The spacing between the chains in the vorticity direction also shows periodicity. The chains slide relative to each other due to a slight displacement in the X (velocity gradient) direction and advection by the imposed shear flow (see Movie 3 in [51]). Interestingly, the chain offset along X fluctuates in time, but despite these fluctuations, the order in the Z (flow) direction persists (see also Fig. 1 in [51]). The chaining occurs when starting from a random RBC/capsule distribution in 3D. Two closely located parallel chains repel each other but still preserve their structures (see Movie 4 in [51]). Increasing the volume fraction results in the formation of infinite 2D lattices. The crystal configuration assembles from random initial conditions (Movie 5 in [51]). At a high volume fraction, disorder prevails. Figure 2 summarizes the phase behavior.

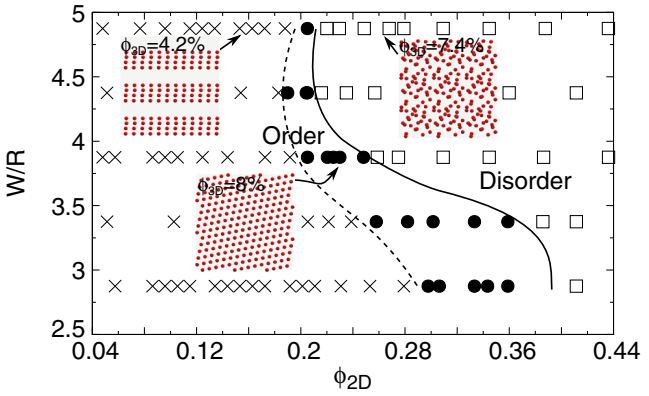

FIG. 2. Phase diagram of order and disorder varying RBC concentration and confinement. $\phi_{2D} = NR^2\pi/(L_Y L_Z)$, where N is the number of particles. The computational domain in Y and Z direction is varied from $8R$ to $18R$ for different cases. The computational domain for the insets is $L_Y = L_Z = 18R$. Displayed are 3×3 computational domains.

In addition to linear chains, numerically, we discovered other configurations. We explored the stability of other possible configurations (Fig. 3), in order to probe the existence of crystalline structures other than one-dimensional (1D) chains. The simulations show that the final stable configurations are all symmetric about the flow direction. These elementary crystal configurations serve as building blocks to larger crystals and imply the existence of two types of crystals: (a) a 1D crystal corresponding to an infinite chain, and (b) a 2D crystal based on the triangular arrangements in Fig. 3. This triangular arrangement is also observed in experiments [Fig. 1(c) and Fig. 1 in [51] for the whole image].

Effect of cell deformability.—An important ingredient for the emergence of order to be discussed below is the wall-induced migration that requires cell deformation [57–59]. For a spherical particle, there is no cross-streamline migration in the Stokes regime, owing to the linearity of the Stokes equations. We analyzed the impact of cell deformability on the emergence of order (Fig. 4). Our simulations show that rigid particles never settle in the midplane (due to the absence of wall-induced migration), and disorder prevails; solid spheres, even if initially placed on the midplane, drift apart. This is illustrated by the simulation in Fig. 4, where a disordered pattern is obtained. Moreover, Fig. 4(b) shows that the distance between two given rigid particles increases with time without saturation (solid line), whereas the same quantity shows saturation (indicating stable pairing) when deformable cells are considered (dashed line).

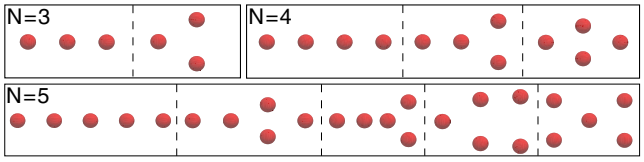

FIG. 3. Ordered stable patterns (in ZY projection) of 3, 4, and 5 interacting particles with confinement of $W = 2.9R$. The computational domain is $L_Y = 18R$, $L_Z = 25R$.

Experiments on hardened RBCs also confirm the lack of order [Fig. 4(a)]. These results support the idea that the wall-induced migration, due to particle deformability, plays a crucial role in the ordering process. Note that, in the presence of inertia, even a spherical particle will undergo a wall-induced migration, allowing ordered patterns of rigid particles to be stabilized [22]. Inertia is also responsible for the hydrodynamic ordering of rotating disks [26] and the strong focalization of capsule suspensions [45] in a pressure-driven flow. Inertia, however, is negligible in our study.

Flow structure around a single cell and around a pair.—Let us now focus on the basic understanding of the crystal formation. We first analyze the flow field around a single cell. Figure 5(a) illustrates the flow around the particle in the X-Z (shear) plane. Figure 5(b) shows that in the Y-Z plane, this flow field is quadrupolar in nature. Figures 5(c) and 5(d) zoom into the flow and show the existence of recirculation zones, nonexistent in unconfined shear flow [34,60,61]. Their centers are designated as elliptic points (EPs) hereafter. The center of a TT cell also constitutes an EP. Between two EPs, there is a point where the flow, locally, is hyperbolic [Fig. 5(c)]. This point is referred to as hyperbolic point (HP). In Fig. 5(a), these points are located where four colors meet. Movie 6 in [51] experimentally illustrates the existence of a HP close to a single TT RBC. The EPs are essential for the formation of RBC chains, as suggested earlier [41]. The triangular structure in Fig. 3 can be inferred from the quadrupolar field structure. The leftmost particle tries to attract the two symmetrically disposed ones towards alignment, whereas these two particles repel each other in the vertical directions. The interplay between attraction and repulsion stabilizes this

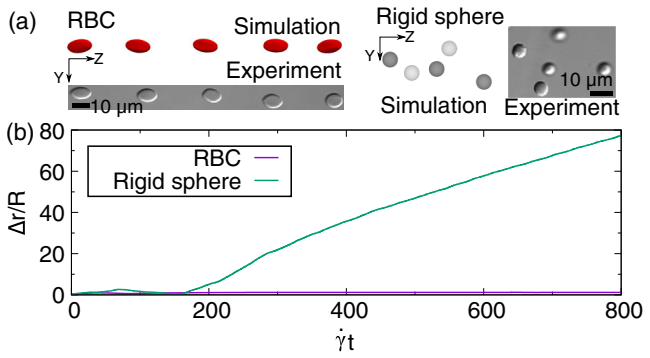

FIG. 4. (a) Configurations for deformable cells after a long time: Simulation, $W = 4.9R$, $\mathrm{Re} = 0.05$, $L_Y = 12R$, $L_Z = 37.5R$; Experiment, $W = 4.9R$, $C_{as} = 0.7$, $\mathrm{Re} \sim 10^{-5}$. Configurations for rigid spheres after a long time: Simulation, $W = 4.5R$, $\mathrm{Re} = 0.05$, $L_Y = L_Z = 18R$; Experiment, $W = 4.5R$, $\mathrm{Re} \sim 10^{-5}$. (b) Distance between two particles as a function of time: the dashed line corresponds to deformable cells, while the solid line corresponds to rigid spheres, or hardened RBCs.

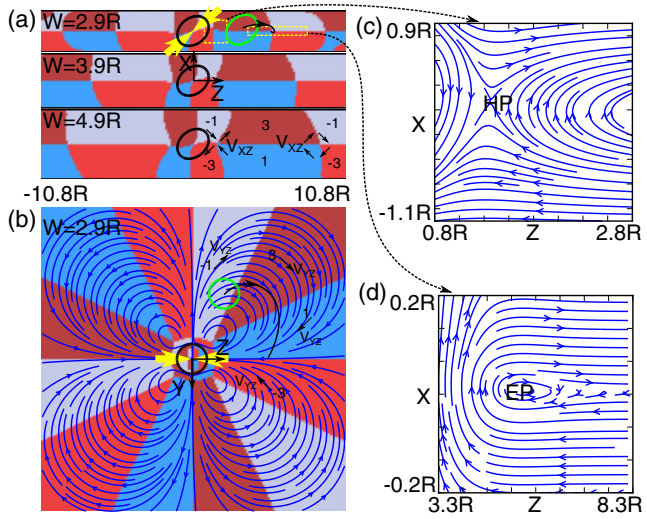

FIG. 5. (a) In the shear plane, the color code shows the value of $\mathrm{Col} = V_Z/|V_Z| + 2V_X/|V_X|$. The gray, dark red, blue, and red colors correspond to $\mathrm{Col} = -1$, 3, 1, -3, respectively. -1 refers to $V_X < 0$ and $V_Z > 0$, 3 to $V_X > 0$ and $V_Z > 0$, 1 to $V_X > 0$ and $V_Z < 0$, and -3 to $V_X < 0$ and $V_Z < 0$. The intersections of the four colors alternatively show EPs and HPs. The streamlines at EP and HP are shown in the right panel (c) and (d). The black solid line with an arrow shows the schematic trajectory of the cell represented by the green contour, interacting with the cell represented by the black contour. The computational domain is $L_Y = 36R$, $L_Z = 36R$ in all of these cases. (b) The flow field around a single cell performing TT in the midplane. The cell resists stretching by exerting a force dipole (yellow arrows). The color code shows Col, with X being substituted by Y.

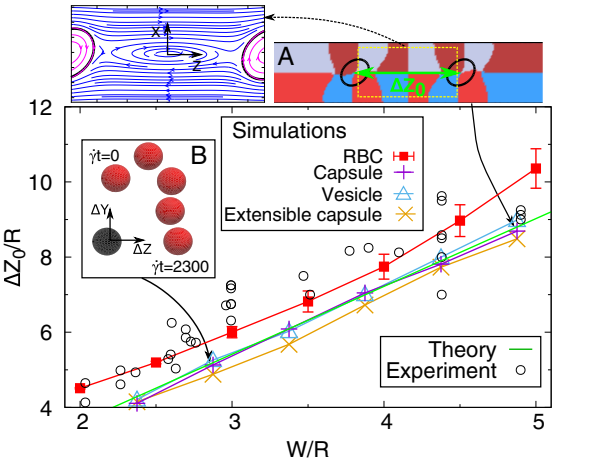

FIG. 6. Equilibrium distance of two cells as a function of gap width $L_Y = 18R$, $L_Z = 36R$ for the simulations of capsules and $L_Y = 12R$, $L_Z = 27R$ for the simulations of RBCs. Error bars in the simulation result from the fact that RBCs "swing," causing small oscillations of the equilibrium distance. Insets: (a) The flow field in the shear plane when two capsules form a stable pair (capsules are shown by black ellipses). $L_Y = L_Z = 36R$. And (b), the evolution of two capsules with time showing the attraction and ultimate formation of a stable pair. Here, $W = 2.9R$, $L_Y = L_Z = 18R$.

configuration. Figure 6(a) shows the flow field after a stable pair is formed [(a) left panel; see also Movie 7 in [51]] and Fig. 6(b) shows an example of the trajectory of the pairing cells [(b) inset]. A comparison with Fig. 5(a) shows (i) that in pair formation the second cell settles close to the EPs created by the first cell (see also the analytical theory below) and (ii) that between a cell pair there are two HPs and one EP.

If pair formation is studied at different confinements, an almost linear dependence of the equilibrium pair distance ΔZ_0 with channel width is observed, Fig. 6. The experimental data are in good agreement with RBC simulations, and it is slightly above the capsule simulations and theory (see below). This indicates that the small reduced volume of RBCs causing their elongation also contributes to the equilibrium distance.

Analytical theory for pair formation.—A detailed analysis of this phenomenon (see theory in [51]) shows that the pairing results from an intricate interplay between (i) a long-range hydrodynamic attraction of two cells along the flow direction, (ii) the wall-induced migration across the streamlines, and (iii) a short range hydrodynamic repulsion between the cells due to the imposed shear flow (since the cell mass centers are not exactly on the midplane, their relative translational velocity is nonzero; thus the shear flow is acting to separate the pair). As dictated by the translational invariance along Y, the coordinates of the cells in the pair can be written as $(-\Delta X, 0, 0)$ and $(\Delta X, 0, \Delta Z)$. The question amounts to determining the steady-state and stable positions ΔX_0 and ΔZ_0.

A steady-state solution corresponds to zero velocity for both cells (the pair of cells is at rest in the laboratory frame). The Z (flow-direction) component of the velocity of a cell in a pair has two contributions: (i) the velocity field induced by the first cell and (ii) the unperturbed shear flow. The first effect can be well approximated by the quadrupolar flow field shown in Fig. 5(b). This flow field has a monotonic algebraic decay (see [51]) as the distance between the two cells increases. The red curve in Fig. 7 shows the location where the total (quadrupolar + imposed shear) contribution to the Z component of the velocity vanishes in the $(\Delta X, \Delta Z)$ plane.

The X (velocity-gradient direction) component of the velocity of a cell in the pair has two contributions: (i) the flow induced by the other cell and (ii) the wall-induced migration across the streamlines. The first contribution has a complicated form [52], which can be well approximated by a rapidly-decaying attenuated sine wave (theory in [51]). The second contribution is proportional to the cell displacement from the midplane (theory in [51]). Equating the sum of these contributions to zero gives a second relation between ΔX and ΔZ, shown by the blue curve in Fig. 7.

The intersections of the blue and the red curves in Fig. 7 correspond to the stationary separations of the two cells.

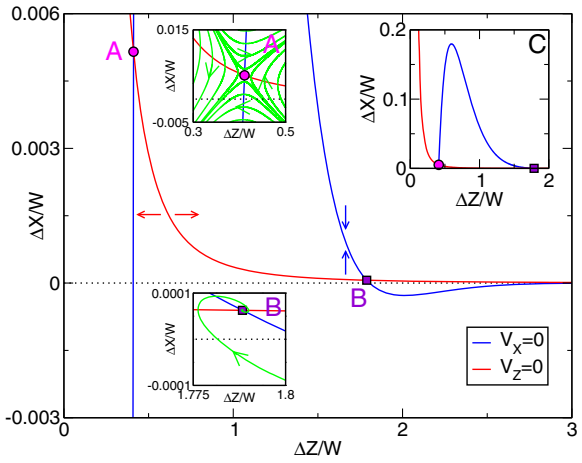

FIG. 7. Theoretical analysis of relative motion of two cells in confined shear flow. The cells are located in positions $(-\Delta X, 0, 0)$ and $(\Delta X, 0, \Delta Z)$. Blue (red) curve marks the separations for which the X (Z, respectively) component of the velocity of the cells vanishes. Crossing the blue (red) curve exchanges the cell interaction along the X (Z, respectively) direction between attraction and repulsion, as shown by the blue (red, respectively) arrows. The intersections of the red and the blue curves correspond to stationary separations. The magenta circle (point A) corresponds to the unstable separation. The violet square (point B) corresponds to the stable separation. The black dotted line corresponds to the case when both cells are in the midplane. Inset (a): Orbits of the separation $[\Delta X(t), 0, \Delta Z(t)]$ in the vicinity of the unstable stationary separation (point A). Arrows indicate the direction in which the separation evolves with time. Inset (b): An orbit of the separation $[\Delta X(t), 0, \Delta Z(t)]$ in the vicinity of the stable stationary separation (point B). The arrow shows that the separation converges to the stationary value with time. Inset (c): Red and blue curves at a larger scale.

Two such intersections can be identified: The separation corresponding to point A in Fig. 7 is unstable, as suggested by the orbits in Fig. 7(a). The separation corresponding to the point B is stable, as suggested by the orbit in Fig. 7(b).

For weak confinement $W/R \gg 1$, we deduce an asymptotic scaling law (see [51])

$$\Delta Z_0/W \simeq 1.805. \tag{1}$$

This scaling is universal as it is independent of the details of the cell structural parameters. Details of the physical nature of the cell (e.g., reduced volume, elastic properties, etc.), or its precise shape, show up only in the correction terms [51] to the main scaling given above. Equation (1) provides a very good agreement with the full numerical simulation (Fig. 6). In order to highlight the universal behavior, we have run other simulations for vesicles (pure phospholipid membranes) and extensible capsules (see [51]). The equilibrium distance is shown in Fig. 6, and it agrees well with the other simulations.

Linear stability analysis shows stability (attraction along the Y direction) with a spiral trajectory in the X-Z-plane (two complex eigenvalues), as shown schematically in Fig. 7(b). The complex nature of the eigenvalues leads to a spiraling of the trajectory towards the stable fixed point [Fig. 7(b)].

Conclusions.—Our work highlights the key roles of cell deformability and shape in the emergence of order. The analytical theory points to cross-stream migration of the cells as the driving force of cell-cell pairing and eventual multi-cell ordering. Our study suggests that the difference in the structuring ability of healthy (deformable) and diseased (stiff) RBCs creates a flow signature potentially exploitable for the detection and analysis of blood diseases that are accompanied by decreased cell deformability, e.g., sickle cell anemia.

We are very grateful to V. Marchenko for many stimulating discussions. We thank Q. Xie, M. Wouters, and D. Hessling for the help in numerics. C. M., A. F., and Z. S. thank the CNES (Centre National d'Etudes Spatiales) for partial financial support and the French-German University Programme "Living Fluids" (Grant No. CFDA-Q1-14). T. F. thanks the LIPhy laboratory, where the experimental work was performed, for financial support. The CPU time was provided by the HLRS (High-Performance Computing Center Stuttgart).

*chaouqi.misbah@univ-grenoble-alpes.fr

[1] T. Vicsek and A. Zafeiris, Phys. Rep. **517**, 71 (2012).
[2] W. Bialek, A. Cavagna, I. Giardina, T. Mora, E. Silvestri, M. Viale, and A. M. Walczak, Proc. Natl. Acad. Sci. U.S.A. **109**, 4786 (2012).
[3] J. L. Silverberg, M. Bierbaum, J. P. Sethna, and I. Cohen, Phys. Rev. Lett. **110**, 228701 (2013).
[4] M. C. Marchetti, J. F. Joanny, S. Ramaswamy, T. B. Liverpool, J. Prost, M. Rao, and R. A. Simha, Rev. Mod. Phys. **85**, 1143 (2013).
[5] A. Zottl and H. Stark, Phys. Rev. Lett. **112**,118101 (2014).
[6] A. M. Menzel, Phys. Rep. **554**, 1 (2015).
[7] A. Snezhko, Curr. Opin. Colloid Interface Sci. **21**, 65 (2016).
[8] O. D. Lavrentovich, Curr. Opin. Colloid Interface Sci. **21**, 97 (2016).
[9] H.-P. Zhang, A. Be'er, E.-L. Florin, and H. L. Swinney, Proc. Natl. Acad. Sci. U.S.A. **107**, 13626 (2010).
[10] C. Dombrowski, L. Cisneros, S. Chatkaew, R. E. Goldstein, and J. O. Kessler, Phys. Rev. Lett. **93**, 098103 (2004).
[11] J. Palacci, C. Cottin-Bizonne, C. Ybert, and L. Bocquet, Phys. Rev. Lett. **105**, 088304 (2010).
[12] Z. Izri, M. N. van der Linden, S. Michelin, and O. Dauchot, Phys. Rev. Lett. **113**, 248302 (2014).
[13] C. A. Weber, T. Hanke, J. Deseigne, S. Leonard, O. Dauchot, E. Frey, and H. Chate, Phys. Rev. Lett. **110**, 208001 (2013).
[14] N. Kumar, H. Soni, S. Ramaswamy, and A. K. Sood, Nat. Commun. **5**, 4688 (2014).
[15] K. Feitosa and N. Menon, Phys. Rev. Lett. **88**, 198301 (2002).

[16] A. Bricard, J.-B. Caussin, N. Desreumaux, O. Dauchot, and D. Bartolo, Nature (London) **503**, 95 (2013).
[17] G. Kokot, S. Das, R. G. Winkler, G. Gompper, I. S. Aranson, and A. Snezhko, Proc. Natl. Acad. Sci. U.S.A. **114**, 12870 (2017).
[18] M. Driscoll, B. Delmotte, M. Youssef, S. Sacanna, A. Donev, and P. Chaikin, Nat. Phys. **13**, 375 (2017).
[19] T. Beatus, R. Bar-Ziv, and T. Tlusty, Phys. Rev. Lett. **99**, 124502 (2007).
[20] M. Baron, J. Bławzdziewicz, and E. Wajnryb, Phys. Rev. Lett. **100**, 174502 (2008).
[21] W. Lee, H. Amini, H. A. Stone, and D. Di Carlo, Proc. Natl. Acad. Sci. U.S.A. **107**, 22413 (2010).
[22] K. J. Humphry, P. M. Kulkarni, D. A. Weitz, J. F. Morris, and H. A. Stone, Phys. Fluids **22**, 081703 (2010).
[23] I. Shani, T. Beatus, R. H. Bar-Ziv, and T. Tlusty, Nat. Phys. **10**, 140 (2014).
[24] K. Yeo, E. Lushi, and P. M. Vlahovska, Phys. Rev. Lett. **114**, 188301 (2015).
[25] E. Lushi, H. Wioland, and R. E. Goldstein, Proc. Natl. Acad. Sci. U.S.A. **111**, 9733 (2014).
[26] Y. Goto and H. Tanaka, Nat. Commun. **6**, 5994 (2015).
[27] F. da Cunha and E. Hinch, J. Fluid Mech. **309**, 211 (1996).
[28] H. Zhao, E. S. Shaqfeh, and V. Narsimhan, Phys. Fluids **24**, 011902 (2012).
[29] X. Grandchamp, G. Coupier, A. Srivastav, C. Minetti, and T. Podgorski, Phys. Rev. Lett. **110**, 108101 (2013).
[30] R. G. Henríquez Rivera, K. Sinha, and M. D. Graham, Phys. Rev. Lett. **114**, 188101 (2015).
[31] T. Beatus, T. Tlusty, and R. Bar-Ziv, Nat. Phys. **2**, 743 (2006).
[32] T. Beatus, R. H. Bar-Ziv, and T. Tlusty, Phys. Rep. **516**, 103 (2012).
[33] W. E. Uspal and P. S. Doyle, Soft Matter **8**, 10676 (2012).
[34] P. Janssen, M. Baron, P. Anderson, J. Blawzdziewicz, M. Loewenberg, and E. Wajnryb, Soft Matter **8**, 7495 (2012).
[35] W. E. Uspal and P. S. Doyle, Soft Matter **10**, 5177 (2014).
[36] K. B. Migler, Phys. Rev. Lett. **86**, 1023 (2001).
[37] J. A. Pathak and K. B. Migler, Langmuir **19**, 8667 (2003).
[38] J. L. McWhirter, H. Noguchi, and G. Gompper, Proc. Natl. Acad. Sci. U.S.A. **106**, 6039 (2009).
[39] J. L. McWhirter, H. Noguchi, and G. Gompper, New J. Phys. **14**, 085026 (2012).
[40] G. Tomaiuolo, L. Lanotte, G. Ghigliotti, C. Misbah, and S. Guido, Phys. Fluids **24**, 051903 (2012).
[41] T. Fischer and P. Richardson, in *1980 Advances in Bioengineering*, American Society of Mechanical Engineers, edited by V. Mow (United Engineering Center, New York, 1980), pp. 305–308.
[42] B. Bull, C. Feo, and M. Bessis, Cytometry **3**, 300 (1983).
[43] J. A. Pathak, M. C. Davis, S. D. Hudson, and K. B. Migler, J. Colloid Interface Sci. **255**, 391 (2002).
[44] T. Krüger, S. Frijters, F. Günther, B. Kaoui, and J. Harting, Eur. Phys. J. Spec. Top. **222**, 177 (2013).
[45] T. Krüger, B. Kaoui, and J. Harting, J. Fluid Mech. **751**, 725 (2014).
[46] E. Jiang Ding and C. K. Aidun, Phys. Rev. Lett. **96**, 204502 (2006).
[47] L. Shi, T.-W. Pan, and R. Glowinski, Phys. Rev. E **86**, 056308 (2012).
[48] T. Krüger, B. Kaoui, and J. Harting, J. Fluid Mech. **751**, 725 (2014).
[49] A. Laadhari, P. Saramito, and C. Misbah, Phys. Fluids **24**, 031901 (2012).
[50] T. Fischer, M. Stöhr-Liesen, and H. Schmid-Schönbein, Science **202**, 894 (1978).
[51] See Supplemental Material at http://link.aps.org/supplemental/10.1103/PhysRevLett.120.268102 for details of the analytical model and movies, from experiments and simulations, illustrating pattern formation and RBC behaviors, which includes Refs. [51–55].
[52] N. Liron and S. Mochon, J. Eng. Math. **10**, 287 (1976).
[53] D. Marenduzzo, E. Orlandini, M. E. Cates, and J. M. Yeomans, Phys. Rev. E **76**, 031921 (2007).
[54] P. M. Vlahovska, T. Podgorski, and C. Misbah, C.R. Phys. **10**, 775 (2009).
[55] C. Pozrikidis, *Boundary Integral and Singularity Methods for Linearized Viscous Flow* (Cambridge University Press, Cambridge, 1992).
[56] A. Farutin and C. Misbah, Phys. Rev. Lett. **110**, 108104 (2013).
[57] I. Cantat and C. Misbah, Phys. Rev. Lett. **83**, 880 (1999).
[58] U. Seifert, Phys. Rev. Lett. **83**, 876 (1999).
[59] S. Sukumaran and U. Seifert, Phys. Rev. E **64**, 011916 (2001).
[60] M. Zurita-Gotor, J. Bławzdziewicz, and E. Wajnryb, J. Fluid Mech. **592**, 447 (2007).
[61] J. L. McWhirter, H. Noguchi, and G. Gompper, Proc. Natl. Acad. Sci. U.S.A. **106**, 6039 (2009).